RSC Advances

PAPER

View Article Online
View Journal | View Issue

Cite this: *RSC Adv.*, 2023, **13**, 11171

Ultrasonic-assisted synthesis of magnetic recyclable Fe_3O_4/rice husk biochar based photocatalysts for ciprofloxacin photodegradation in aqueous solution

Tran Quoc Toan,[a] Nguyen Thi Mai,[bc] Hoang Minh Trang,*[b] Pham Van Hao[d] and Dang Van Thanh*[e]

Received 10th January 2023
Accepted 30th March 2023

DOI: 10.1039/d3ra00178d

rsc.li/rsc-advances

In this work, a new facile one-spot method has been designed to fabricate a magnetic recyclable Fe_3O_4/rice husk biochar photocatalyst (FBP) for the removal of Ciprofloxacin (CIP) in aqueous solution. This method combines ultrasonic-assisted impregnation and precipitation, which can overcome the difficulties of long-time reactions, complex procedures, and extreme condition requirements. The successful fabrication of the Fe_3O_4/biochar material has been proven by a series of material characterization techniques, including X-ray diffraction (XRD), Scanning Electron Microscopy (SEM), Raman, Fourier Transform Infrared Spectroscopy (FTIR), X-ray Photoelectron Spectroscopy (XPS), and vibrating sample magnetometer (VSM). Moreover, the as-product FBP exhibited the excellent ability of photodegrading CIP and the possibility of magnetic recovery from the aqueous solution, suggesting a potential solution for removing antibiotic pollutants in environmental remediation.

1. Introduction

Ciprofloxacin (CIP) is one of the 2nd-generation fluoroquinolone antibiotics. Possessing broad-spectrum antibacterial activity, CIP is known as one of the most powerful antibiotics in the fluoroquinolone group, and is used to treat many bacterial infections such as respiratory tract infections, urinary tract infections, intestinal tract infections (diarrhea, typhoid…).[1] Currently, CIP-involved treatment has been experiencing increasing antibiotic-resistance-related troubles due to antibiotic abuse, especially in developing countries.[2,3] The elimination of antibiotics in general and CIP, in particular, is significant since the antibiotic residues in water are harmful to some microorganisms, enabling many wastewater treatment bioprocesses and can worsen antibiotic resistance status. As a result, various techniques have been developed and used to remove antibiotics, such as adsorption, biofilm, photocatalytic degradation, advanced oxidation, Fenton, *etc.*[4] Among them, ultraviolet (UV) or visible light photocatalysis are of great interest thanks to its high removal efficiency and environmental friendliness.[5–7] Consequently, many types of photocatalytic materials have been developed to remove CIP, for example, metal oxide materials with nanostructures or their combinations such as TiO_2/biochar, Zn-doped Cu_2O, ZnO/biochar.[8–11] The difficulty in recovery of these materials, however, is one of its major drawbacks. Centrifugation and filtration are two favorable solutions in laboratory-scale but hardly to be implemented in industrial wastewater systems due to its cost and complex process. In addition, the other disadvantages which limiting the dissemination of these materials is the high cost and time consuming of its manufacturing process. Therefore, developing methods to produce affordable materials possessed both efficient CIP removal and its rapid and easily separation from the aqueous phase is a gap need to be filled in order to balancing the efficiency and the effectiveness in upscaled implementation.

Recently, biochar is a highly porous material produced from the pyrolysis of raw materials derived from plant biomass or agricultural by-products (corn stalks, peanut shells, wood shells, rice husks, livestock, and poultry manure) in anaerobic conditions.[12,13] Biochar is widely used in various fields, such as agricultural cultivation (soil improvement, moisture preservation) and environmental pollution treatment (adsorbent, catalyst, catalyst carrier) because of its like-activated-carbon properties.[14] This approach has promoted research on converting wastes into biochar and its application in environmental

[a]*Faculty of Chemistry, Thai Nguyen University of Education, 20 Luong Ngoc Quyen, Thai Nguyen, Vietnam*

[b]*Faculty of Environmental Sciences, University of Science, Vietnam National University, Hanoi, 334 Nguyen Trai Road, Hanoi, Vietnam. E-mail: hoangminhtrang@hus.edu.vn*

[c]*Faculty of Basic Science, Thai Nguyen University of Agriculture and Forestry, Quyet Thang ward, Thai Nguyen city, Thai Nguyen, Vietnam*

[d]*TNU-University of Information and Communication Technology, Z115 St., Quyet Thang Ward, Thai Nguyen City, Thai Nguyen, Vietnam*

[e]*Faculty of Basic Science, Thai Nguyen University of Medicine and Pharmacy, 284 Luong Ngoc Quyen, Thai Nguyen city, Thai Nguyen, Vietnam. E-mail: thanhdv@tnmc.edu.vn*

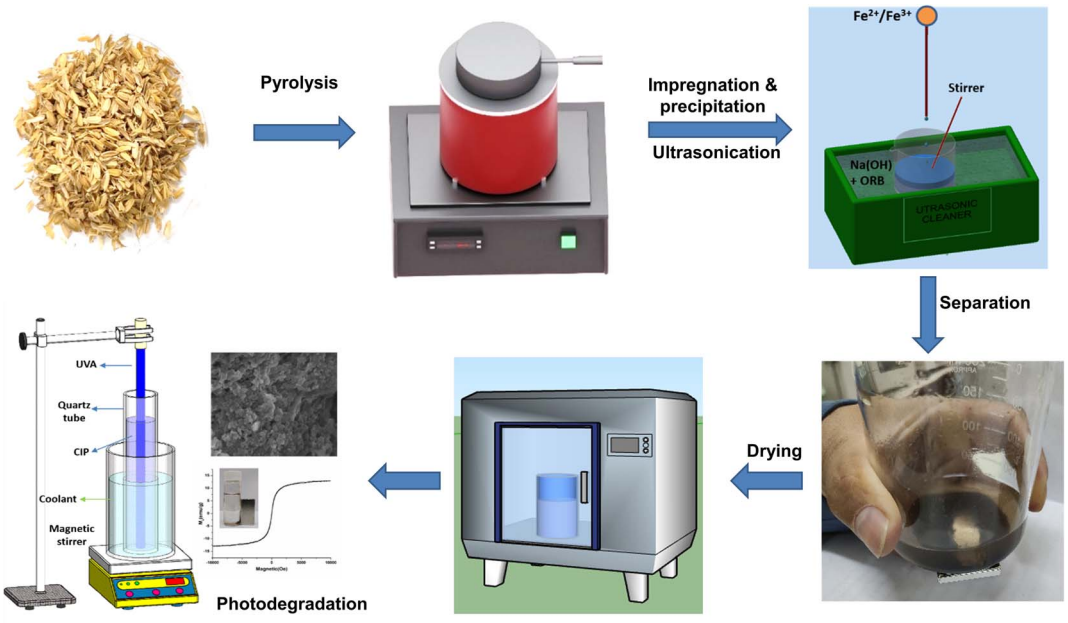

Fig. 1 The schematic representation of the preparation processes and CIP photodegradation.

treatment or agricultural cultivation to achieve two goals simultaneously: biomass-derived waste treatment and environmental pollution treatment, creating soil improvement materials. However, the small particle size of biochar makes it challenging to separate from the aqueous environment after treatment and often requires filtration and centrifugation, which are expensive and complex processes that hinder their application in large-scale wastewater treatment systems. Thus, various methods have been developed to solve this bottleneck, such as thermochemical, co-precipitation, reductive co-deposition, and mechanical milling *via* incorporating Fe_3O_4 nanoparticles on biochar.[15–17] This combination could minimize the limitations of each material and help promote their superior properties, especially in treating contaminated water. For example, Ayoub *et al.* used Fe^{2+}/Fe^{3+} mixture to modify waste camel bone biochar, prepared a magnetic nanocomposite, and explored its adsorption properties for the adsorption of toxic metals from water.[18] For modifying purposes, the impregnation and/or precipitation through a chemical reaction of ferrous/ferric precursors with biochar is often employed thanks to its simple procedure.[16,19] On the other hand, the exploitation of ultrasonication to promote and shorten reaction time has been widely introduced in nanomaterial synthesis, especially for Fe_3O_4 or hybrid materials.[20–22] Thanks to the cavitation effect, the bubbles, which are generated by ultrasonic, create locally high temperatures (*e.g.*, 10 000 K) and pressures (*e.g.*, 10 000 atm), which might lead to some interesting physicochemical effects, especially in synthesizing of nano-compounds.[22,23] This can produce Fe_3O_4 nanoparticles with a high saturation magnetization of about 80 emu g^{-1}, which was approximate to bulk Fe_3O_4 at room temperature without any heat treatment.[24] As demonstrated, the ultrasonic-assisted approach has been favorable for the formation of hybrid or nanomaterials without using any additional chemical reagents or apparatus.[25] To the best of our knowledge, a simple coupling ultrasonic-assisted impregnation and precipitation is a reasonable method to produce magnetic recyclable Fe_3O_4/biochar photocatalysts from rice husk for ciprofloxacin photodegradation in an aqueous solution.

In this work, we explore a novel facile process to fabricate the magnetic recyclable Fe_3O_4/rice husk biochar based photocatalysts (MFBP) which coupling ultrasonic-assisted impregnation and precipitation reaction and study its applicability for CIP photodegradation. The as-prepared MFBP possesses a large specific surface area thanks to the cavitation effect, thus raising contact site of MFBP with CIP molecules and improving the separation of photogenerated electron–hole pairs and acceleration interfacial charge transfer. The results prove that MFBP is an effective photocatalyst for treating CIP-contained wastewater and promote research on converting residues agricultural biomass into biochar and its application in environmental remediation.

2. Materials and methods

2.1. Materials

Rice husk were collected from rice factories in Thai Nguyen province. The chemicals, including KH_2PO_4 (≥99.0%, Merck), ciprofloxacin (analytical standard, Merck), $FeSO_4 \cdot 7H_2O$ (≥99.0%, Merck), $Fe_2(SO_4)_3 \cdot xH_2O$ (97%, Merck), NaOH (≥85.0%, Merck) and HNO_3 (70%, Merck) were used for experiments without further purification. All experiments were performed using deionized (DI) water and double-distilled (DD) water.

2.2. Methods

2.2.1. Fabrication of FBP. Rice husks were washed thoroughly with double distilled water and dried till their moisture

was below 5% before being pyrolyzed in anaerobic condition at 800 °C for 1 hour. After let it cooled down, rice husk biochar was washed with DD water followed by drying at 80 °C for 12 hours; the product was unmodified biochar, denoted as ORB.

A mass of 5 g ORB was weighed and placed in a 1000 mL beaker, then 300 mL of NaOH 0.5 M was poured into this beaker to create a mixture. This mixture was slowly added to 300 mL of a solution containing $FeSO_4 : Fe_2(SO_4)_3$ at a molar ratio of 4 : 1 with a concentration of 0.5 M, which had been being sonicated and stirred (at speed of 10 rpm) for 60 minutes. The resulting precipitate powder was collected by a magnet, washed several times with DI water until pH 7, then dried in a vacuum oven at 60 °C for 4 hours; the product was denoted as UFBP. For comparison, the sample without ultrasonic was named FBP. Also, the postfixes of 5, 10 and 15 are used to indicate the mass of biochar in grams which were used in the preparation procedure. The schematic representation of the preparation processes is presented in Fig. 1.

2.2.2. Study the photocatalytic ability of UFBP. The photocatalytic activity of materials was evaluated by the degradation of CIP in the solution (initial concentration of 10 mg L^{-1}) under UVA illumination, as demonstrated in Fig. 1. To eliminate the effect of ambient light, the whole experimental setup was placed in a dark room, and the reaction temperature was maintained at 25 °C using water as a coolant. The experiments were conducted as follows: weigh 150 mg of materials and put into a measuring cylinder containing 250 mL of CIP 10 mg L^{-1} with pH 5.5. Firstly, the mixtures were magnetically stirred for 60 minutes in the dark to achieve adsorption–desorption equilibrium. Then, the mixtures were magnetically stirred and illuminated by UVA lamps for 180 minutes, and a volume of 1.5 mL was sampled every 30 minutes. The solid samples were separated using a magnet, and liquid phases were determined by photometric method at an absorption wavelength of 276 nm using Hitachi UH5300 UV-VIS Double Beam Spectrophotometer.

2.2.3. Antibacterial activity study. Both Gram-positive bacteria and Gram-negative bacteria are sensitive to Ciprofloxacin. Thus, to determine the antibacterial activity of CIP, the antibacterial zone measurement method was employed with Gram-positive bacteria *Bacillus subtilis* (BS) and Gram-negative bacteria *Escherichia coli* (*E. coli*). The antibacterial activity of CIP was determined based on the formation of antibacterial zones on the Petri dish of medium, surrounding the assay containing each of the tested solutions, including CIP solution prior to photocatalysis and CIP solution later to 120, 180, and 240 minutes of photocatalysis. The bacterial volume of 100 μL with a density of approximately 10^6 CFU mL^{-1} was equally distributed on the surface of Peri dishes containing Luria Bertani Broth (LB). The assays of 8 mm in diameter were punched on the surface of medium, where 50 μL of desired solutions were pipetted into. These LB-Peri dishes were incubated at 30 °C for 24 hours before the diameter measurement of the antibacterial zone. Each experiment was replicated three times.

2.2.4. Scavenger experiments. These experiments were carried out to investigate the generation of reactive oxygen species during the photocatalytic process using UFBP catalyst. Appropriated volumes of Ethylene diamine tetraacetic acid (EDTA), Isopropyl alcohol (IPA) and Ascorbic acid (AA) were used as the scavengers for hydroxyl radical ($^{\bullet}OH$), h^+, superoxide ($O_2^{\bullet -}$) in 250 mL of the reaction solution.

2.2.5. Characterization. X-ray diffraction patterns (XRD) and Raman spectra of samples were recorded on X-ray diffractometer (D2 PHASER) and Labram HR evolution Raman spectrometer, respectively. The morphological characteristics of samples were surveyed by scanning electron microscope JEOL JSM-6700F SEM. The specific surface area of the samples was determined by measuring N_2 adsorption isotherm on the Tri Star 3000 instrument at 77 K. Magnetic saturation was determined using the MicroSense EZ9 vibrating sample magnetometer. The chemical bonds of samples were investigated by XPS (Escalab 250Xi, Thermo Scientific) and FTIR (Nicolet iS50 FTIR spectrometer), respectively. Electrochemical impedance spectra (EIS) were recorded using a three-electrode electrochemical workstation and the flat band of samples were determined using Autolab workstation PGS 302N. The working electrode was fabricated by dripping 100 μL of a mixed solution of UFBP, carbon black, and polyvinylidene difluoride (PVDF) with the ratio 80 : 10 : 10 in *N*-methyl pyrrolidinone solvent at a concentration of 10 mg mL^{-1} on FTO substrate (with the surface area of 1 cm^2) then dried at 40 °C for 48 hours. The electrolyte Na_2SO_4 1 M was used for EIS measurements. The intermediates of CIP photodegradation were detected by LC-MSD-Trap-SL Agilent 1100.

3. Results and discussion

Fig. 2 illustrates XRD, Raman and FT-IR spectra of raw materials (Fe_3O_4, ORB) and obtained catalyst (UFBP). It can be observed that the characteristic peaks revealed at $2\theta = 30.05°$; 35.36°; 43.08°; 57.07° and 62.68° corresponding to the planes (220), (311), (400), (511) and (440) of Fe_3O_4 (JCPDS 19-0629) as shown in Fig. 2a. Meanwhile, the characteristic peaks of ORB occurred at $2\theta = 22.14°$, 29.42°, and 43.61°, corresponding to the planes (002), (220), and (100) of amorphous carbonaceous carbon.[26] Notably, when combines with each other, the peaks of both materials appeared at $2\theta = 30.05°$; 35.36°; 43.08°, corresponding to the planes (002), (220) and (311) with the lower intensity of diffraction peaks. To further confirm, FTIR spectra of ORB, Fe_3O_4 and UFBP were recorded, and results are presented in Fig. 2c. It is clearly shown that the spectrum of ORB contains characteristic peaks at the wavelengths of 1047 cm^{-1}, 678 cm^{-1} and 452 cm^{-1} corresponding to the stretching oscillatoric asymmetric bonding Si–O–Si. The peak at 1567 cm^{-1} indicates the appearance of the C=C (sp^2) bond.[27] Meanwhile, Fe_3O_4 spectrum has characteristic peaks at 629 cm^{-1} and 583 cm^{-1}, corresponding to the stretching oscillatory of the Fe–O bonds in the lattice of iron oxide.[18] The peaks at 1625 cm^{-1} and a wide peak at 3416 cm^{-1} are associated with the appearance of the flexed hydroxyl (-OH) and stretched –OH groups. For UFBP, the characteristic peaks of both Fe_3O_4 and ORB at 623 cm^{-1} and 787 cm^{-1} were revealed. Moreover, the optical absorption properties of UFBP were evaluated using UV-vis absorption spectra and the band gap (E_g) was estimated by employing the Kubelka–Munk equation is $E_g = 1.81$ eV (Fig. 2d). The UFBP

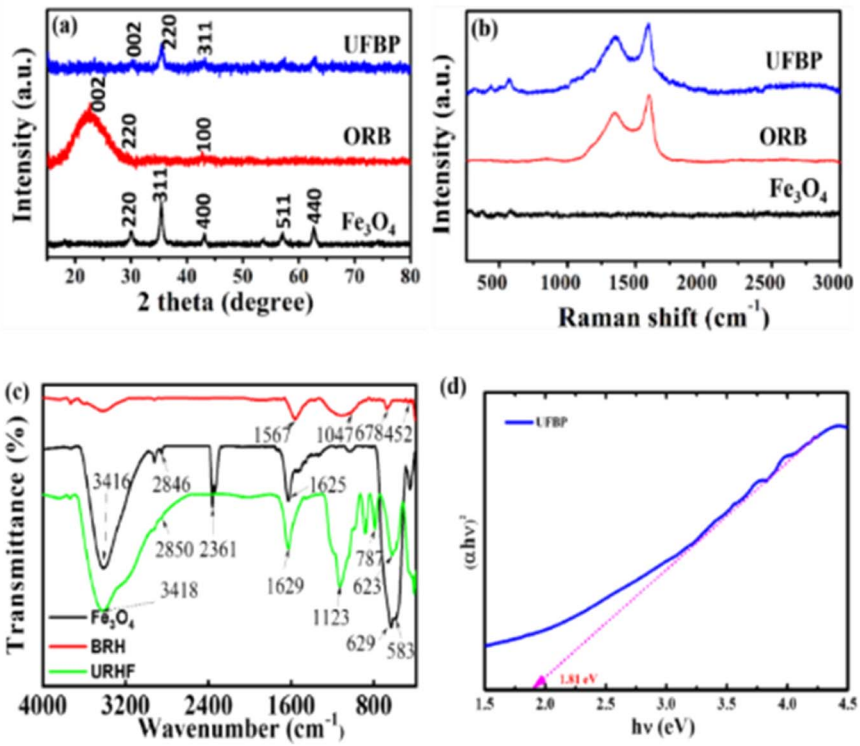

Fig. 2 (a) XRD, (b) Raman, (c) FTIR spectra of Fe_3O_4, ORB, UFBP and (d) the band gap of UFBP.

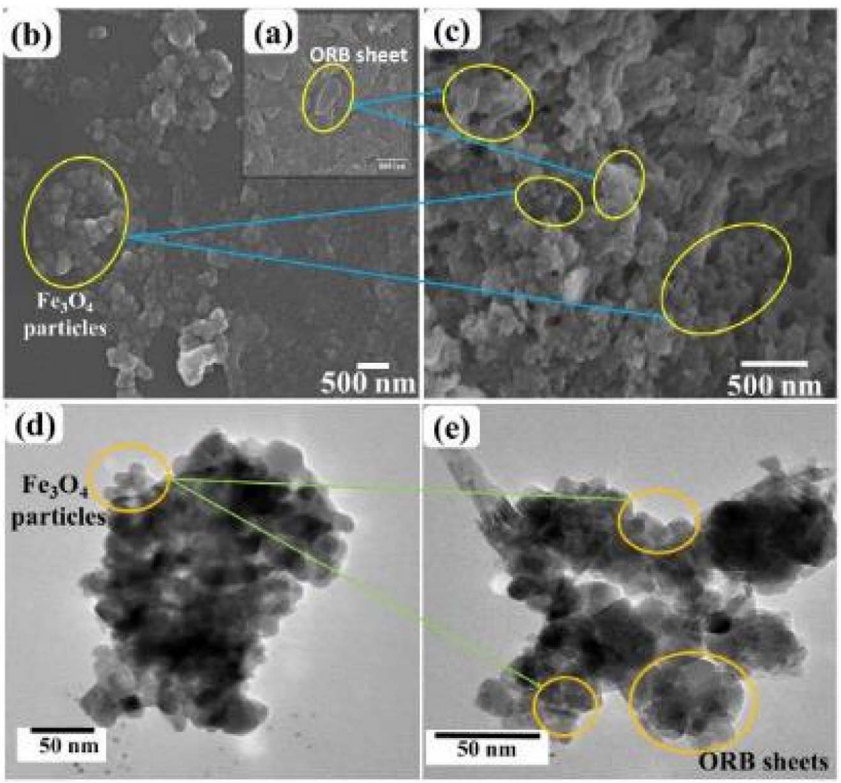

Fig. 3 (a–c) SEM images of ORB, Fe_3O_4, UFBP and (d, e) TEM images of Fe_3O_4, UFBP.

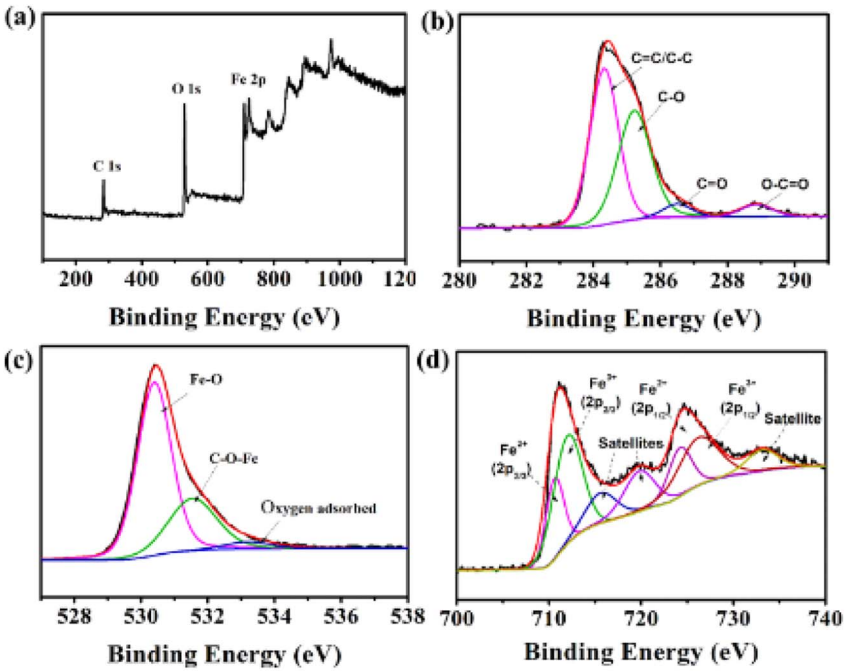

Fig. 4 (a) Survey, (b) C 1s, (c) O 1s and (d) Fe 2p XPS spectra of UFBP.

sample with a narrow band gap which performs better light absorption that produces more photoinduced charge carriers in the photocatalytic process.

The SEM and TEM images as shown in Fig. 3 described the morphology of ORB, Fe_3O_4 and UFBP. It can be seen from SEM images (Fig. 3a) the original form of ORB was the large sheets,

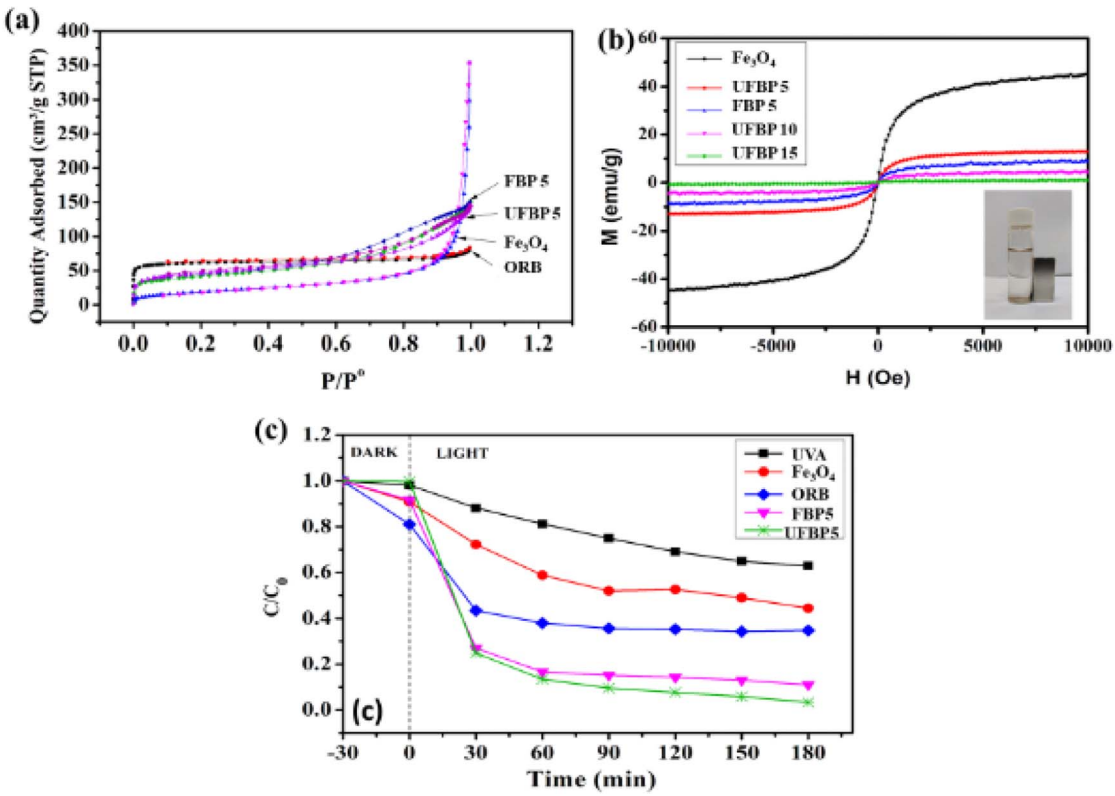

Fig. 5 (a) Nitrogen adsorption isotherms of ORB, Fe_3O_4, UFBP5, FBP5, (b) magnetization hysteresis loop of Fe_3O_4, FBP5, UFBP5, 10, 15 and (c) CIP photocatalytic degradation performance in the presence of UVA, Fe_3O_4, ORB, FBP5, UFBP5 under UVA, initial concentration 10 mg L^{-1}, pH 5.5, 25 °C, rotation speed 300 rpm; inset in (b) is an image demonstrating the magnetic separation of UFBP5 from solution.

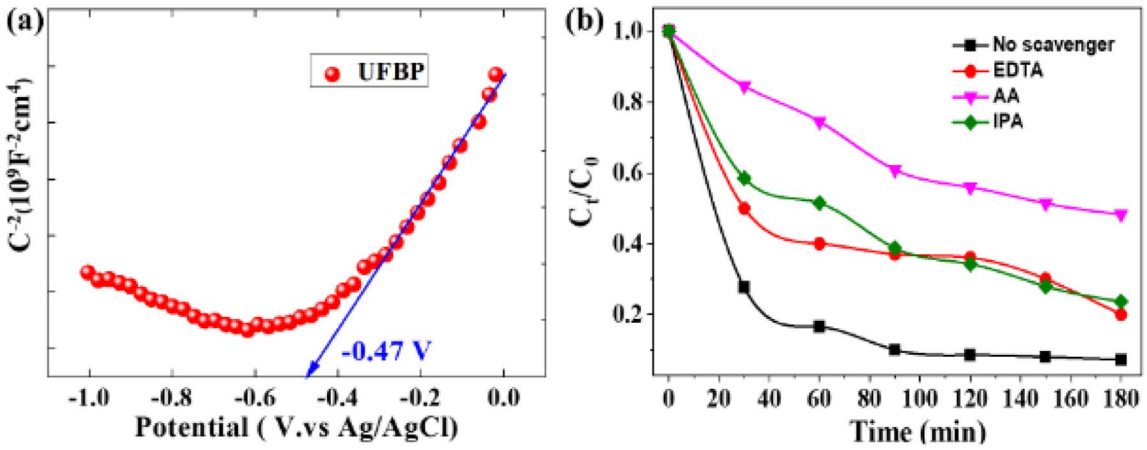

Fig. 6 (a) Mott–Schottky plots plotted as C-2 referenced to the Ag/AgCl electrode for UFBP; (b) photocatalytic degradation of CIP by UFBP under visible light irradiation and in the presence of scavengers: EDTA, AA, and IPA.

while Fe_3O_4 was in the form of nanoparticles (Fig. 3b). After the magnetization, UFBP (Fig. 3c) possesses a rougher surface due to the ORB biochar fragments were coated in Fe_3O_4 nanoparticles. TEM images also indicated Fe_3O_4 existed in nanoparticles form with size of 15–20 nm (Fig. 3d) which then alternated with ORB sheets as seen in Fig. 3e. These existences prove the combination of two ingredients in the resulted material and is elucidated by results from XPS analysis of UFBP (Fig. 4).

As seen in Fig. 4a, the survey scan of UFBP indicates the existence of C, O, Fe elements. The C 1s XPS spectrum of UFBP (Fig. 4b) is ascribed to non-oxygenated C (C–C/C=C), epoxy (C=O), carbonyl (C–OH), carboxylate (O–C=O).[28] Additionally, O1s spectrum (Fig. 4c) can be de-convoluted into three peaks at a binding energy of 529.70 eV, 531.21 eV, and 532.25 eV ascribed to Fe–O bonds, C–O-iron bond, and oxygen defects/oxygen adsorbed on the surface of samples,[29,30] respectively. The high-resolution Fe 2p (Fig. 4d) spectrum shows two peaks at binding energies of 711.4 eV and 724.9 eV, which are attributed to Fe 2p3/2 and Fe 2p1/2, respectively. In addition, a satellite peak was observed at 717.00 eV, confirming the presence of high crystalline Fe_3O_4 in the samples. The calculation of the

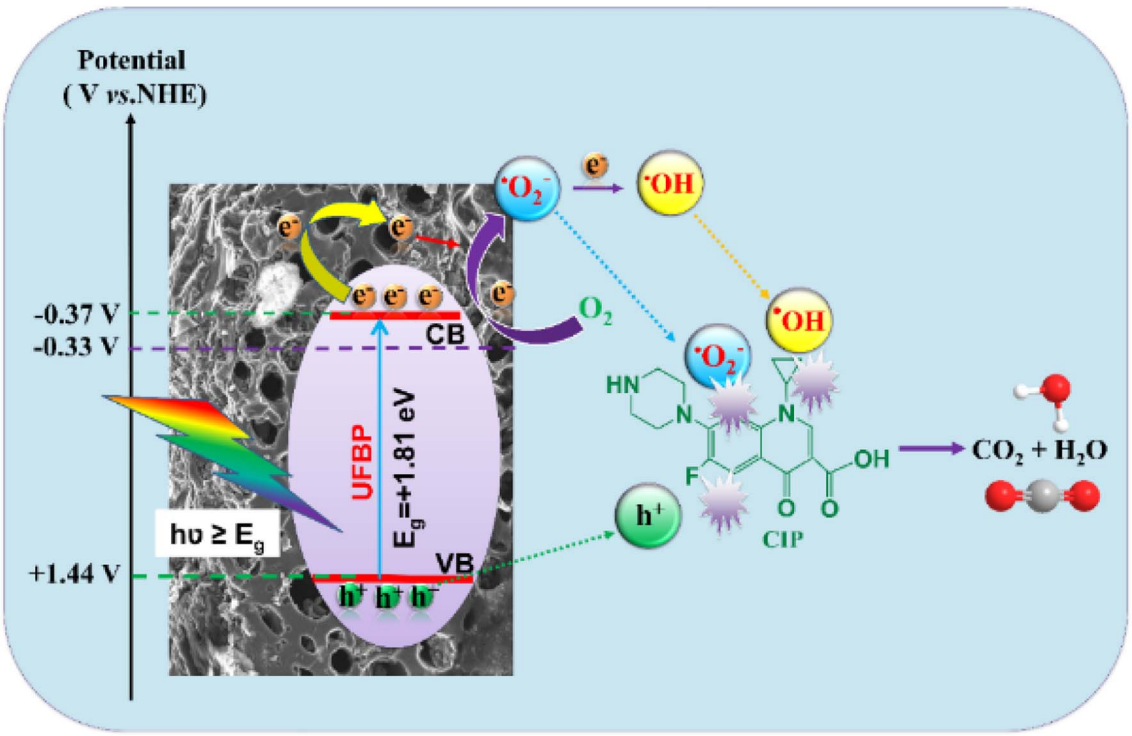

Fig. 7 Schematic diagram of conduction band (CB) and valence band (VB) potentials of UFBP.

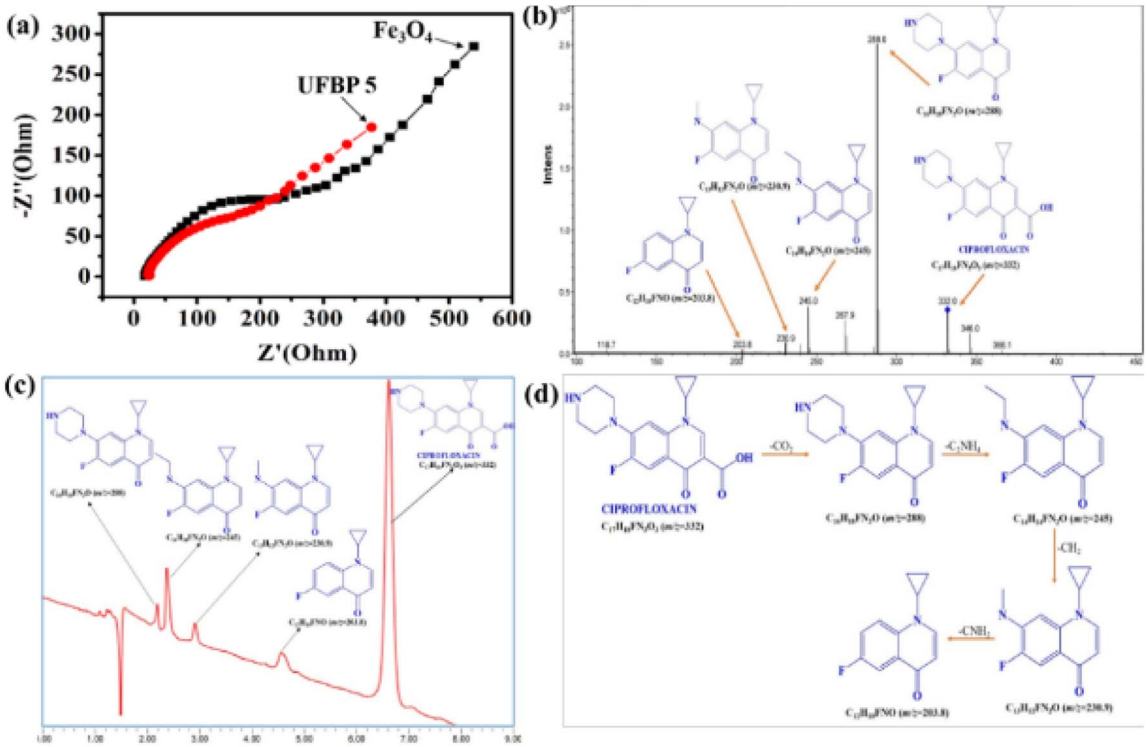

Fig. 8 (a) EIS of Fe_3O_4 and UFBP5, (b) HPLC, (c) LC/MS and (d) possible mechanism of CIP photodegradation after 180 min.

area of Fe^{2+} : Fe^{3+} peak gives the ratio of 0.51, which is consistent with the relative theoretical composition of Fe^{2+} : $Fe^{3+} = 0.5$ in Fe_3O_4 structure.[31] The higher ratio from the peak compared to the theoretical value also confirmed the existence of Fe_2O_3 phase as presented by XRD analysis, which agrees with the satellite peak at 716.2 eV.

Consequently, these results confirmed the successful formation of a magnetic hybrid through the decoration of Fe_3O_4 on the ORB using the combination of ultrasonic-assisted impregnation and precipitation reaction (Fig. 5). The bond between biochar and ferromagnetic oxide can be occupied between Fe–OH on the surface of iron oxides and C–OH on the surface of biochar, as evidenced in XPS and FTIR results. To further elucidate, the magnetization hysteresis loop and BET (Fig. 5a) of Fe_3O_4 and hybrid samples were recorded. As shown in Fig. 5b, all samples almost quickly reached saturation in relation to paramagnetic characteristics. The magnetic saturations of UFBP5 (13.02 emu g^{-1}), FBP5 (8.86 emu g^{-1}), UFBP 10 (4.52 emu g^{-1}) and UFBP15 (0.91 emu g^{-1}) were smaller than that of Fe_3O_4 sample (45.21 emu g^{-1}) due to the addition of carbon in the hybrid material. However, the Ms of UFBP5 was high enough for magnetic separation from aqueous media, as shown in Fig. 5b. Thus, the UFBP5 was selected for further studies. The potential application of the UFBP5 is evaluated through the photodegradation of CIP under UVA light. For comparison, the treatments by ORB, Fe_3O_4, and direct photolysis (only UVA light) were also performed. As shown in Fig. 5c photodegradation efficiency was within the range of 37.2%, 55.5%, and 65.3% for 180 min under UVA light irradiation without photocatalyst, Fe_3O_4, and with ORB, respectively. When it was irradiated using UFBP5, photodegradation efficiency significantly increased to 96.7%. Notably, FBP5 also revealed a fairly good photodegradation ability of CIP but smaller than that of UFBP5 due to lower BET (Fig. 5a). Moreover, Ms of UFBP5 is larger than that of FBP5 (Fig. 5b) as a result of the inhibiting agglomeration of Fe_3O_4 and increasing BET (Fig. 5a) due to ultrasonic irradiation effect in the preparing procedure. From the results, it may be concluded that the Fe_3O_4 molecules interacted with the carbon sheets to form a magnetic recyclable Fe_3O_4/biochar photocatalyst, which possesses a large specific surface area and high potential of recovery and reuses after the treatment process.

To clarify the photocatalytic reaction mechanism of UFBP, Mott–Schottky analysis, the band structure of UFPB was determined. As displayed in Fig. 6a, the flat bands (EFB) of UFBP is −0.47 V *vs.* Ag/AgCl. It is noteworthy that the slope of UFBP is positive, which means that UFBP is n-type photocatalyst. Moreover, the Efb of the n-type semiconductor is about 0.1 V lower than its the CB minimum.[32] The CB potential of UFBP is estimated to be −0.37 V *vs.* NHE, by the following equation: $E_{NHE} = E_{Ag/AgCl} + 0.197$ V. Based on the equation of $E_g = E_{VB} - E_{CB}$, the valence band (VB) top of UFPB is determined to be +1.44 V.

To confirm the formation of reactive species, the scavenger studies for free radicals of the photoctalytic system were also investigated due to its effect on reaction time, pathways, and final products in photocatalytic reactions.[33] As illustrated in Fig. 6b, EDTA, IPA and AA were employed as quenching agents

to elucidate the production of radicals, including hole (h^+), hydroxyl ($^{\bullet}OH$), superoxide anion ($O_2^{\bullet-}$), respectively. The variation of C_t/C_0 of UFBP can be considered as a function of irradiation time before and after adding to scavengers of free radicals. The photocatalytic degradation of CIP in the presence of scavengers are 48.63% for AA, 23.70% for IPA and 20.30% for EDTA. The results clarify that hole (h^+) and $O_2^{\bullet-}$ and $^{\bullet}OH$ are the primary reactive species for CIP photocatalytic degradation into the non-toxic compound, H_2O, and CO_2.

Based on the above experiment, the possible mechanism of Fe_3O_4/rice husk biochar material is proposed in Fig. 7. When a UVA light is incident on the photocatalyst material, UFBP releases photo-generated hole–electron pairs. The photoexcited electrons of UFBP migrate to CB while the holes transfer to the VB. The photogenerated electrons transfer from the conduction band of Fe_3O_4 to the empty orbital of the graphene-like structure biochar through conjugated π-bond molecules or direct transfer biochar, leading electron–hole pairs to separate more easily and the charge recombination rate to decrease, then improving photocatalytic efficiency. In addition, the electronic charges in CB can easily reduce O_2 to generate $O_2^{\bullet-}$ (EH = 0.33 V *versus* NHE), then continuously generate $^{\bullet}OH$. Eventually, $O_2^{\bullet-}$, $^{\bullet}OH$ and holes can directly react with the CIP to degrade them into non-toxic products.

$$\text{UFBP} + h\nu \text{ (photon energy)} \rightarrow e_{CB}^- + h_{VB}^+$$

$$e_{CB}^- + O_2 \rightarrow O_2^{\bullet-}$$

$$O_2 + 2e^- + 2H^+ \rightarrow H_2O_2$$

$$H_2O_2 + e^- \rightarrow {}^{\bullet}OH$$

$$h_{VB}^+, {}^{\bullet}OH, O_2^{\bullet-} + \text{CIP} \rightarrow CO_2 + H_2O$$

Afterward, enhancing the performance towards CIP photodegradation of UFBP5 was compared to Fe_3O_4 as a result of raising contact site of UFBP5 with CIP molecules and transfer capacity of photogenerated electrons. To verify, EIS measurement was conducted for evaluation of the charge transfer resistance and the separation efficiency of charge carriers. As shown in Fig. 8a, the arc radius (EIS Nyquist plot) of the UFBP5 was smaller than those of Fe_3O_4. Typically, the semicircle diameter in the high frequency region reflected the charge transfer resistance between the electrode and the electrolyte.[34–36] Thus, these results clearly elucidated more effective separation of photogenerated electron–hole pairs and accelerated interfacial charge transfer from UFBP5 to reaction molecules than that from Fe_3O_4. Besides, the intermediates formed during the photodegradation of CIP by UFBP5 were

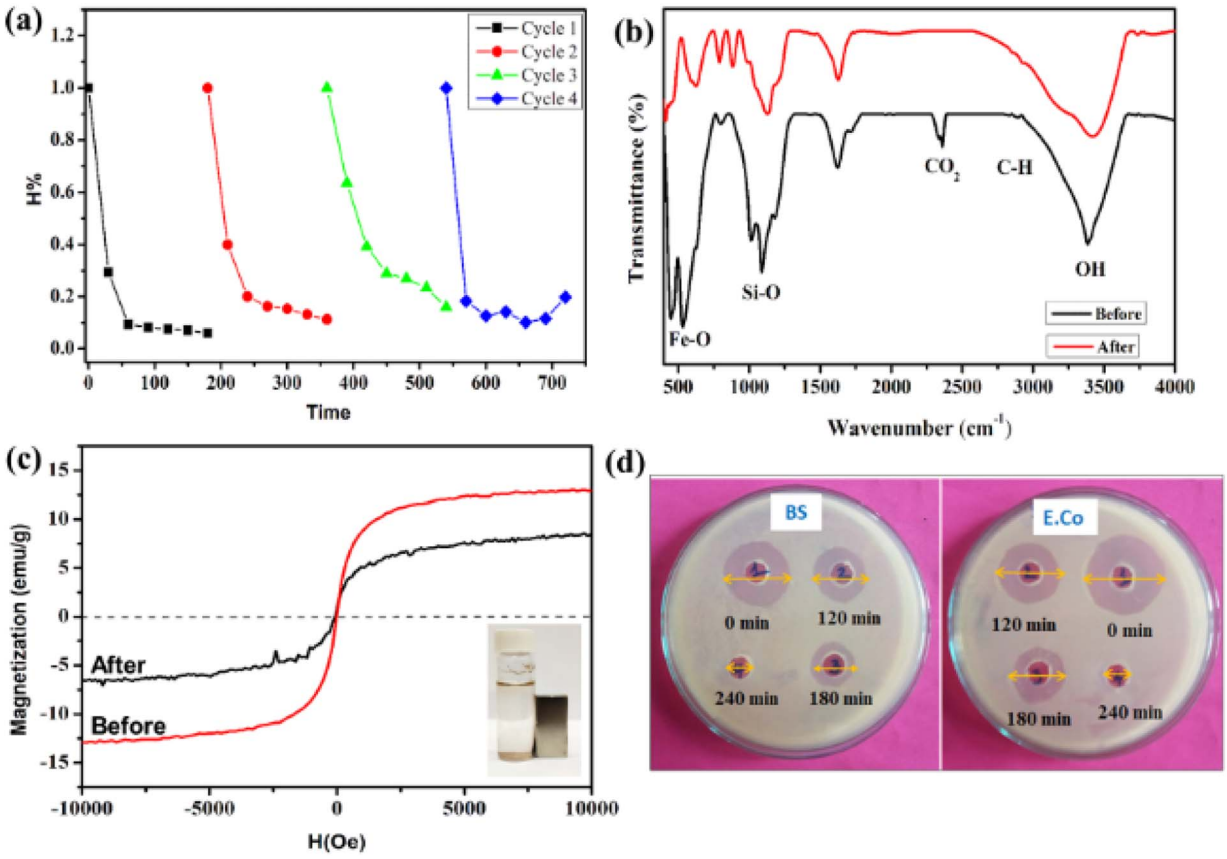

Fig. 9 (a) CIP photodegradation efficiency of reusing UFBP5 material, (b) FTIR and (c) VSM of UFBP5 before and after four recycle photodegradation; (d) diameters of antibacterial zones *Bacillus subtilis* and (k) *Escherichia coli* at the different time of UVA illumination with the presence of UFBP5; inset in (c) is an image of UFBP5 magnetic separation from solution after 4th recycle.

Table 1 Comparison of the photocatalytic ability of several Fe_3O_4-containing photocatalysts

No.	Photocatalyst	Pollutant	Contact time (min)	Efficiency (%)	Ref.
1	Fe_3O_4@TiO_2-PVP shell	Congo red dye	120	78.2	37
2	Fe_3O_4/CuO	Direct red 89	240	89	38
3	Fe_3O_4	Cibacron red FN-R	100	85.51	39
4	Fe_3O_4/SnO_2	*p*-Chlorophenol	300	89	40
5	Fe_3O_4/SiO_2/TiO_2 core-2-layer-shell nanocomposite	Ciprofloxacin	120	94	41
6	UFBP	Ciprofloxacin	180	96.7	This research

Table 2 Antibacterial activity of CIP after photocatalysis time

	Diameter of the antibacterial zone (mm)			
Bacteria	(1) After 0 minute	(2) After 120 minutes	(3) After 180 minutes	(4) After 240 minutes
Bacillus subtilis (BS)	16.5 ± 0.1	11.4 ± 0.2	4.2 ± 0.1	0
Escherichia coli (E.co)	19.4 ± 0.2	13.5 ± 0.1	9.1 ± 0.1	0

determined by LC/MS analysis (Fig. 8b) and further confirmed by HPLC data (Fig. 8c). The probable intermediates of the CIP photodegradation with corresponding *m*/*z* values are presented in Fig. 8c, and the possible pathway for this photodegradation is proposed as follows: Firstly, the molecular structure of CIP could be lost $-CO_2$ of a carboxylic group leading to a high-intensity signal appearance at $m/z = 288$ which corresponds to the molecular ion $[C_{16}H_{18}FN_3O]^+$. One prominent fragment ion is observed at $m/z = 245$ (corresponding to ion $[C_{14}H_{14}FN_2O]^+$) by destroying the N1 and N4 positions of the piperazine ring (losing the $-C_2NH_4$ group). The $[C_{14}H_{14}FN_2O]^+$ molecular ion ($m/z = 245$) can undergo further loss of $-CH_2$ group belonging to the remaining part of the piperazine ring, forming a molecular ion $[C_{13}H_{12}FN_2O]^+$ ($m/z = 230.8$) which finally lost $-CNH_2$ group of piperazine part to obtain the fragment ion $[C_{12}H_{10}FNO]^+$ ($m/z = 203.8$).

The reusability of the material is vital to the evaluation of the material's practical applicability. The UFBP5 material, after photocatalytic treatment, was recovered through magnetic attracting, washed several times with DI water, then dried in the oven. The results of CIP degradation efficiencies after four cycles of reusing material are presented in Fig. 9a. As can be seen, the photocatalytic activity of UFBP5 was fairly well maintained, revealed by degradation efficiency was 94.03% for the first-turn test and 80.24% after the fourth turn, including minor changes in the FTIR spectra (Fig. 9b) and Ms. The decrease of the photodegradation efficiency and Ms was attributed to the loss of some of the catalysts through withdrawing, consumption in the photocatalytic degradation. Notably, the UFBP5 after the fourth turn still maintains the easy magnetic separation as observed in Fig. 9c. It is proved that UFBP5 material has a high potential to reuse and recover and is an economical solution in the treatment of CIP residues in water. Moreover, the comparison of the photocatalytic ability in our research with others is shown in Table 1. It was found that the photocatalytic efficiency of UFBP was effective and higher than the figures of most Fe_3O_4-containing photocatalysts which were exhibited in previous papers. Besides that, the reaction time is average in comparison with other samples. Hence, UFBP could be used as a good photocatalyst in the application for the degradation of antibiotics in wastewater.

Additionally, the toxicity of CIP solution prior and latter to the photodegradation by UFBP5 under UVA irradiation (Fig. 9d) is further investigated by assessing the growth of *Bacillus subtilis* (BS) and *Escherichia coli* (E.co) since BS and E.co are both indicators for various environments and sensitive to CIP. These post-treatment antibacterial activity assessment of the antibiotic photodegraded intermediates provide the basis to identify their environmental effects. The antibacterial activities of the CIP solution after 0, 120, 180, and 240 minutes of photocatalysis by UFBP5 were exhibited in the diameter of the antibacterial zone shown in Table 2.

According to these results, the diameter of the antibacterial zone decreased sharply with photocatalysis time, indicating that the antibacterial activity of CIP decreased with time and completely wore off after 240 minutes of photocatalysis. Therefore, when degrading CIP by UFBP5 photocatalyst, the degraded products possessed low antibacterial activity for BS and E.co, indicating the ecological safety of the CIP discharges photodegraded by UFBP5 photocatalyst.

4. Conclusions

Magnetic recyclable Fe_3O_4/rice husk biochar based photocatalysts were successfully fabricated *via in situ* ultrasonic-assisted impregnation and precipitation technique and employed for photocatalytic removal of ciprofloxacin in aqueous solution. This photocatalyst exhibited the ability to remove CIP by photodegradation better than that of Fe_3O_4 as a result of higher surface area and a lower rate of electron–hole

pair recombination. Moreover, it possessed good reusability, with 80.24% of CIP degraded after four cycles. The photo-degraded products reveal a low antibacterial activity which is correlated to high ecological safety. These results provide the potential for large-scale industrial environmental remediation.

Author contributions

T. Q. Toan formally analyzed and wrote original draft. N. T. Mai curated data. D. V. Thanh, H. M. Trang wrote review & editing. D. V. Thanh and P. V. Hao conceived, designed, and supervised for experiments. All authors read and approved the final manuscript.

Conflicts of interest

The authors declare no conflict of interest.

Acknowledgements

The authors would like to thank the Ministry of Education and Training for funding this study *via* a ministerial-level project. Code B2021-TNA-15.

Notes and references

1 B. Nunes, C. Leal, S. Rodrigues and S. C. Antunes, Assessment of ecotoxicological effects of ciprofloxacin in Daphnia magna: life-history traits, biochemical and genotoxic effects, *Water Sci. Technol.*, 2018, **2017**, 835–844.

2 P. T. P. Hoa, S. Managaki, N. Nakada, H. Takada, A. Shimizu, D. H. Anh, P. H. Viet and S. Suzuki, Antibiotic contamination and occurrence of antibiotic-resistant bacteria in aquatic environments of northern Vietnam, *Sci. Total Environ.*, 2011, **409**, 2894–2901.

3 T. Truong, H. D. Bui, T. T. V. Pham, L. T. Tran, D. H. Nguyen, C. Ng and T. H. Le, Occurrences of antibiotic resistant bacteria in a tropical river impacted by anthropogenic activities in Ho Chi Minh City, *Int. J. Environ. Sci. Technol.*, 2022, **19**, 7049–7058.

4 X. Yang, Z. Chen, W. Zhao, C. Liu, X. Qian, M. Zhang, G. Wei, E. Khan, Y. Hau Ng and Y. Sik Ok, Recent advances in photodegradation of antibiotic residues in water, *Chem. Eng. J.*, 2021, **405**, 126806.

5 M. Jiménez-Salcedo, M. Monge and M. T. Tena, Study of intermediate by-products and mechanism of the photocatalytic degradation of ciprofloxacin in water using graphitized carbon nitride nanosheets, *Chemosphere*, 2020, **247**, 125910.

6 X. Yu, J. Zhang, J. Zhang, J. Niu, J. Zhao, Y. Wei and B. Yao, Photocatalytic degradation of ciprofloxacin using Zn-doped Cu2O particles: Analysis of degradation pathways and intermediates, *Chem. Eng. J.*, 2019, **374**, 316–327.

7 W. Wang, W. Gao, X. Nie, W. Liu, X. Cheng, N. Shang, S. Gao and C. Wang, Photocatalytic selective amines oxidation coupled with H(2)O(2) production over hyper-cross-linked polymers, *J. Colloid Interface Sci.*, 2022, **616**, 1–11.

8 M. Z. Afzal, P. Zu, C.-M. Zhang, J. Guan, C. Song, X.-F. Sun and S.-G. Wang, Sonocatalytic degradation of ciprofloxacin using hydrogel beads of TiO2 incorporated biochar and chitosan, *J. Hazard. Mater.*, 2022, **434**, 128879.

9 G. Zeng, H. Zhang, S. Liang, X. Zhong, M. Zhang, Z. Zhong, H. Deng, H. Zeng and Z. Lin, Highly efficient photocatalytic degradation of the emerging pollutant ciprofloxacin *via* the rational design of a magnetic interfacial junction of mangosteen peel waste-derived 3D graphene hybrid material, *Environ. Sci.: Nano*, 2022, **9**, 1298–1314.

10 A. O. Egbedina, K. O. Adebowale, B. I. Olu-Owolabi, E. I. Unuabonah and M. O. Adesina, Green synthesis of ZnO coated hybrid biochar for the synchronous removal of ciprofloxacin and tetracycline in wastewater, *RSC Adv.*, 2021, **11**, 18483–18492.

11 L. T. Nguyen, H. T. Nguyen, T.-D. Pham, T. D. Tran, H. T. Chu, H. T. Dang, V.-H. Nguyen, K. M. Nguyen, T. T. Pham and B. Van der Bruggen, UV-Visible Light Driven Photocatalytic Degradation of Ciprofloxacin by N,S Co-doped TiO2: The Effect of Operational Parameters, *Top. Catal.*, 2020, **63**, 985–995.

12 M. B. Ahmed, J. L. Zhou, H. H. Ngo, W. Guo and M. Chen, Progress in the preparation and application of modified biochar for improved contaminant removal from water and wastewater, *Bioresour. Technol.*, 2016, **214**, 836–851.

13 T. T. Cuong, H. A. Le, N. M. Khai, P. A. Hung, L. T. Linh, N. V. Thanh, N. D. Tri and N. X. Huan, Renewable energy from biomass surplus resource: potential of power generation from rice straw in Vietnam, *Sci. Rep.*, 2021, **11**, 792.

14 S. Chandrasekhar, K. G. Satyanarayana, P. N. Pramada, P. Raghavan and T. N. Gupta, Review Processing, properties and applications of reactive silica from rice husk—an overview, *J. Mater. Sci.*, 2003, **38**, 3159–3168.

15 C. Zhao, B. Wang, B. K. G. Theng, P. Wu, F. Liu, S. Wang, X. Lee, M. Chen, L. Li and X. Zhang, Formation and mechanisms of nano-metal oxide-biochar composites for pollutants removal: A review, *Sci. Total Environ.*, 2021, **767**, 145305.

16 J. Qu, J. Shi, Y. Wang, H. Tong, Y. Zhu, L. Xu, Y. Wang, B. Zhang, Y. Tao, X. Dai, H. Zhang and Y. Zhang, Applications of functionalized magnetic biochar in environmental remediation: A review, *J. Hazard. Mater.*, 2022, **434**, 128841.

17 X. Yang, K. Luo, Z. Pi, P. Shen, P. Zhou, L. He, X. Li and Q. Yang, Insight to the mechanism of tetracycline removal by ball-milled nanocomposite CeO_2/Fe_3O_4/biochar: overlooked degradation behavior, *Sep. Purif. Technol.*, 2023, **307**, 122703.

18 L. Yan, S. Li, H. Yu, R. Shan, B. Du and T. Liu, Facile solvothermal synthesis of Fe_3O_4/bentonite for efficient removal of heavy metals from aqueous solution, *Powder Technol.*, 2016, **301**, 632–640.

19 A. S. Eltaweil, H. Ali Mohamed, E. M. Abd El-Monaem and G. M. El-Subruiti, Mesoporous magnetic biochar composite for enhanced adsorption of malachite green dye:

characterization, adsorption kinetics, thermodynamics and isotherms, *Adv. Powder Technol.*, 2020, **31**, 1253–1263.

20 D. Van Thanh, P. P. Oanh and P. H. Le, Ultrasonic-assisted cathodic electrochemical discharge for graphene synthesis, *Ultrason. Sonochem.*, 2017, **34**, 978–983.

21 M. Khatamian, B. Divband and R. Shahi, Ultrasound assisted co-precipitation synthesis of Fe_3O_4/bentonite nanocomposite: performance for nitrate, BOD and COD water treatment, *Journal of Water Process Engineering*, 2019, **31**, 100870.

22 N. N. Huy, V. T. Thanh Thuy, N. H. Thang, N. T. Thuy, L. T. Quynh, T. T. Khoi and D. Van Thanh, Facile one-step synthesis of zinc oxide nanoparticles by ultrasonic-assisted precipitation method and its application for H_2S adsorption in air, *J. Phys. Chem. Solids*, 2019, **132**, 99–103.

23 G. Chatel and R. S. Varma, Ultrasound and microwave irradiation: contributions of alternate physicochemical activation methods to Green Chemistry, *Green Chem.*, 2019, **21**, 6043–6050.

24 Z. Mo, C. Zhang, R. Guo, S. Meng and J. Zhang, Synthesis of Fe_3O_4 nanoparticles using controlled ammonia vapor diffusion under ultrasonic irradiation, *Ind. Eng. Chem. Res.*, 2011, **50**, 3534–3539.

25 B. Jin, P. Bai, Q. Ru, W. Liu, H. Wang and L. Xu, Ultrasonic synthesis of Mn-Ni-Fe tri-metallic oxide anchored on polymer-grafted conductive carbon for rechargeable zinc-air battery, *Ultrason. Sonochem.*, 2021, **81**, 105846.

26 Z. Teng, K. Han, J. Li, Y. Gao, M. Li and T. Ji, Ultrasonic-assisted preparation and characterization of hierarchical porous carbon derived from garlic peel for high-performance supercapacitors, *Ultrason. Sonochem.*, 2020, **60**, 104756.

27 Y. C. Dong, R. G. Ma, M. Jun Hu, H. Cheng, C. K. Tsang, Q. D. Yang, Y. Yang Li and J. A. Zapien, Scalable synthesis of Fe_3O_4 nanoparticles anchored on graphene as a high-performance anode for lithium ion batteries, *J. Solid State Chem.*, 2013, **201**, 330–337.

28 Y. Li, J. Chu, J. Qi and X. Li, An easy and novel approach for the decoration of graphene oxide by Fe_3O_4 nanoparticles, *Appl. Surf. Sci.*, 2011, **257**, 6059–6062.

29 Z. Pan, G. Zhang and X. Wang, Polymeric Carbon Nitride/Reduced Graphene Oxide/Fe_2O_3: All-Solid-State Z-Scheme System for Photocatalytic Overall Water Splitting, *Angew. Chem., Int. Ed.*, 2019, **58**, 7102–7106.

30 F. Wang, L. Xia, X. Li, W. Yang, Y. Zhao and J. Mao, Nano-Ferric Oxide Embedded in Graphene Oxide: High-performance Electrocatalyst for Nitrogen Reduction at Ambient Condition, *Energy Environ. Mater.*, 2021, **4**, 88–94.

31 L. Wan, D. Yan, X. Xu, J. Li, T. Lu, Y. Gao, Y. Yao and L. Pan, Self-assembled 3D flower-like Fe_3O_4/C architecture with superior lithium ion storage performance, *J. Mater. Chem. A*, 2018, **6**, 24940–24948.

32 J. Hou, C. Yang, Z. Wang, W. Zhou, S. Jiao and H. Zhu, In situ synthesis of α–β phase heterojunction on Bi_2O_3 nanowires with exceptional visible-light photocatalytic performance, *Appl. Catal., B*, 2013, **142–143**, 504–511.

33 A. W. Mureithi, Y. Sun, T. Mani, A. R. Howell and J. Zhao, Impact of hole scavengers on photocatalytic reduction of nitrobenzene using cadmium sulfide quantum dots, *Cell Rep. Phys. Sci.*, 2022, **3**, 100889.

34 T.-B. Nguyen, C. P. Huang, R.-a. Doong, C.-W. Chen and C.-D. Dong, Visible-light photodegradation of sulfamethoxazole (SMX) over Ag-P-codoped g-C_3N_4 (Ag-P@UCN) photocatalyst in water, *Chem. Eng. J.*, 2020, **384**, 123383.

35 Y. Liu, Y.-S. Chang, Y.-J. Hsu, B.-J. Hwang and C.-H. Hsueh, Fabrication of WO_3 photoanode decorated with Au nanoplates and its enhanced photoelectrochemical properties, *Electrochim. Acta*, 2019, **321**, 134674.

36 S.-T. Gao, W.-H. Liu, N.-Z. Shang, C. Feng, Q.-H. Wu, Z. Wang and C. Wang, Integration of a plasmonic semiconductor with a metal–organic framework: a case of Ag/AgCl@ZIF-8 with enhanced visible light photocatalytic activity, *RSC Adv.*, 2014, **4**, 61736–61742.

37 S. Sunaryono, D. Fitriana, L. Novita, M. Hidayat, H. Hartatiek, N. Mufti and A. Taufiq, 2020.

38 K. Benabbas, N. Zabat and I. Hocini, Facile synthesis of Fe_3O_4/CuO a core-shell heterostructure for the enhancement of photocatalytic activity under visible light irradiation, *Environ. Sci. Pollut. Res.*, 2021, **28**, 4329–4341.

39 R. Al-Anbari, A. H. Al-Obaidy and E. Abd, Photocatalytic activity of Fe_3O_4 under solar radiation, *Mesopotamia Environmental Journal*, 2016, **2**, 41–53.

40 J. Li, Y. Chen, Q. Wu, J. Wu and Y. Xu, Synthesis of sea-urchin-like Fe_3O_4/SnO_2 heterostructures and its application for environmental remediation by removal of p-chlorophenol, *J. Mater. Sci.*, 2019, **54**, 1341–1350.

41 I. Gabelica, L. Ćurković, V. Mandić, I. Panžić, D. Ljubas and K. Zadro, Rapid microwave-assisted synthesis of Fe_3O_4/SiO_2/TiO_2 core-2-layer-shell nanocomposite for photocatalytic degradation of ciprofloxacin, *Catalysts*, 2021, **11**, 1136.